



Ground subsidence monitoring in based on UAV-LiDAR technology: a case study of a mine in the Ordos, China

Shikai An · Liang Yuan · Ying Xu · Xiao Wang · Dawei Zhou

Received: 30 June 2023 / Accepted: 1 February 2024
© The Author(s) 2024

Abstract Ground subsidence in Western coal mining areas is characterized by rapid deformation, extensive damage, and a wide range of impacts. The conventional observation methods are inappropriate for surface damage monitoring in high-intensity mining areas of Western China. Therefore, it is a crucial problem to quickly, accurately, and comprehensively monitor the ground subsidence and environmental damage caused by high-intensity and large-scale

mining. In this study, we propose a monitoring method for the ground subsidence of high-intensity mining with Unmanned Aerial Vehicle Lidar (UAV-LiDAR) measurement technology. Taking a mine in Ordos of China as an example, the Digital Elevation Model (DEM) is obtained by Kriging Interpolation of the ground point cloud from UAV-LiDAR. Then, the multi-stage DEM differential processing is employed to get ground subsidence. Finally, the median and bilateral filters combine for denoise to obtain the high-precision ground subsidence. The results show that the accuracy of the ground DEM generated by UAV-LiDAR is 15 mm and the mean square error of the ground subsidence basin is 39 mm. UAV-LiDAR technology can quickly obtain abundant surface data and obtain high-precision ground subsidence. Therefore, the application of this technology and method in subsidence monitoring in mining areas is feasible. And it can provide support for ecological environment monitoring, land reclamation, and ecological restoration in mining areas. The research results can provide a useful basis for monitoring the surface damage of coal mining in Western China.

S. An (✉) · L. Yuan

School of Earth and Environment, Anhui University of Science and Technology, Huainan 232001, Anhui, China
e-mail: 330862664@qq.com

S. An

National Engineering Laboratory for Protection of Coal Mine Eco-Environment, Ping An Mining Engineering Technology Research Institute Co., Ltd., Huainan 232001, Anhui, China

L. Yuan

Joint National-Local Engineering Research Centre for Safe and Precise Coal Mining, Anhui University of Science and Technology, Huainan 232001, Anhui, China

Y. Xu

School of Economics & Management, Anhui University of Science and Technology, Huainan 232001, Anhui, China

X. Wang · D. Zhou

School of Environment Science and Spatial Informatics, China University of Mining and Technology, Xuzhou 221116, Jiangsu, China

Article Highlights

1. Analyzed the shortcomings of current conventional monitoring methods for mining subsidence.

2. A UAV Lidar based monitoring of surface deformation in mining areas has been proposed.
3. By this way, a high-precision DEM model can be obtained to obtain more accurate surface subsidence values, making up for the shortcomings of existing research methods.
4. This method has been successfully applied in a mining area in Ordos.

Keywords Coal mining · UAV-LiDAR · DEM · Ground subsidence monitoring · Ground subsidence basin · Median filter, Bilateral filter

1 Introduction

Although coal mining meets Chinese energy demand, it leads to serious geological and environmental damage in the mining area (e.g., rock damage, ground deformation) (Wu et al. 2019). The geological structure of the mining areas in western China has a stable coal seam and suitable conditions for large-scale mechanized mining due to the shallow burial of the coal seam and the fragile geological environment. Indeed, most of the ground subsidence caused by coal mining in the western part showed fast deformation speed, deep damage, and wide range (Ge et al. 2019; Fan et al. 2017). The ground subsidence of the mining area, induced by coal mining activities, can lead to serious geological and environmental problems and even geological disasters (e.g., landslides, mudslides), resulting in serious damage and threats to safe coal mine production and people's lives (Research et al. 2017). The subsidence monitoring in mining areas is of great significance to managing coal mining activities and reducing their negative impact on the ecological environment and the safety of people's lives and property (Hutchinson et al. 1997). The spatiotemporal evolution of ground subsidence caused by the exploitation of mineral resources is a complex process. Studies on ground subsidence law in Western mining areas of China are not comprehensive due to the lack of appropriate subsidence parameters and the fewer ground subsidence monitoring data (He et al. 1991; Ling et al. 1994; Jiwen Bai, et al. 2021; Ma, et al. 2023; Jiwen Bai, et al. 2019.). Indeed, the country's environmental protection requirements are becoming increasingly rigorous, making

environmental monitoring and damage assessment in mining areas major challenges for mining companies in the Western region. Conventional ground subsidence monitoring methods are based on geodetic techniques, such as total station, level measurement, and global positioning system (GPS). These methods consist of monitoring subsidence by laying a directional and inclined observation line on the surface above goaf, using planar coordinates and elevation information of each observatory. These methods have been the most commonly used due to their high accuracy and efficiency in determining surface deformation in mining areas, thus contributing significantly to the research and practical engineering of mine mining subsidence. However, these monitoring methods have the following disadvantages: (1) The monitoring range and scale are small, with a single working surface typically used as the monitoring object; (2) The surface movement deformation is quantified, without considering the environmental damage information (e.g., vegetation, water bodies, etc.); (3) These methods are costly and labor-intensive, the use period is long, and require buried measurement points, which is not practical for long term measurements; (4) Only point observation and little data and information cannot fully reflect the characteristics of subsidence basin (Zhou et al. 2013; Zhang et al. 2016; Aumann et al. 1991). These deficiencies have, indeed, resulted in limited surface damage monitoring in the western high-intensity mining area in China. Therefore, efficient, accurate, and comprehensive monitoring methods of ground subsidence and environmental damage caused by high-intensity large-scale mining in this area are required (Hu and Li 2012).

With the development of low-cost, light unmanned aerial vehicles (UAVs), and technologies in recent years, UAV-LiDAR is a new surveying and mapping technology widely used in monitoring mining areas in geological environments. This technique combines GPS, IMU (Inertial Measurement Unit), and three-dimensional laser LiDAR measurement systems and adapts to multi-scale monitoring applications. It has the advantages of flexible mobility, high efficiency and accuracy, and low operating cost (Lanari et al. 1997; Li et al. 2020). Moreover, UAV-LiDAR does not require buried measurement points in the ground subsidence monitoring of the mining area and can result in high-precision ground subsidence deformation data. At the same time, because

the UAV platform has no occlusion at high altitudes, it can collect more complete surface point cloud data. Therefore, it can avoid the situation that some point cloud data cannot be collected due to terrain fluctuations caused by the ground laser point cloud technology of the same technology. UAV-LiDAR also does not require relocating the station multiple times in the mining area, as is required for ground-based lidar technology. In fact, multiple relocations of the station in a mining area with complex terrain characteristics may significantly increase the registration error during data processing. Compared with the UAV-photogrammetry technology, the beam emitted by LiDAR is penetrable, resulting in more realistic terrain detection and better elevation accuracy without the requirement for image control points. Given these advantages, UAV-LiDAR can play a vital role in ground subsidence monitoring in mining areas in the future (Zhou et al. 2020; Zhou et al. 2014; Kršák et al. 2016; Bai et al. 2017; Qian et al. 2023).

In this study, we propose a monitoring method for the ground subsidence of high-intensity mining with Unmanned Aerial Vehicle Lidar (UAV-LiDAR)

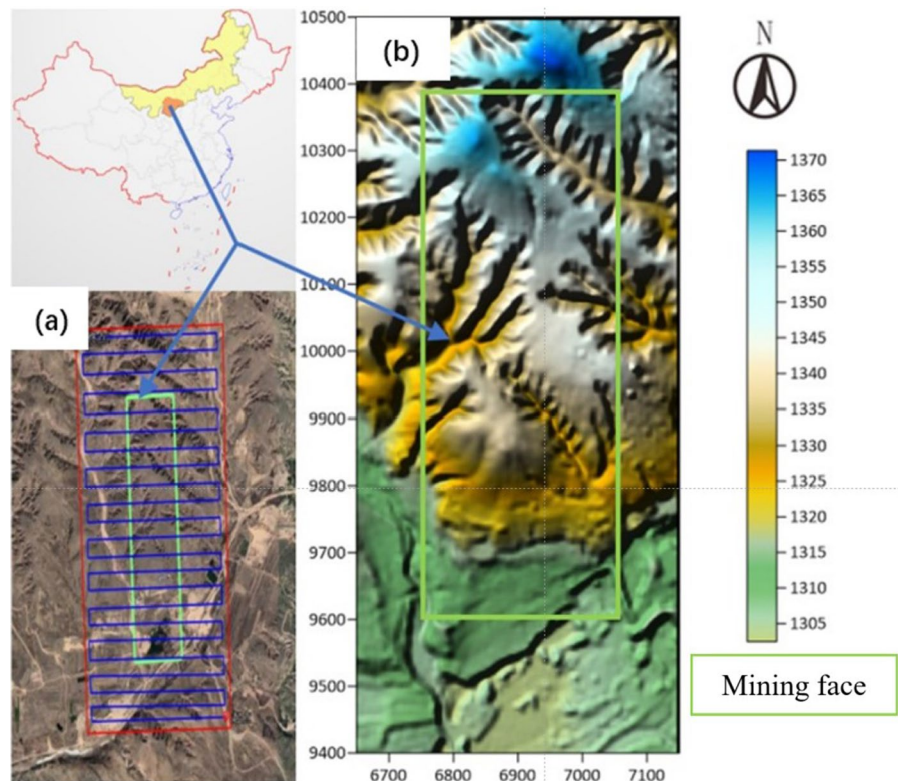
measurement technology. The essential techniques and methods for UAV-LiDAR data acquisition and processing are discussed and analyzed for monitoring ground subsidence of high-intensity mining in Western mining areas in China. The coal mine in Ordos, Inner Mongolia, is selected as the study area. DEM is established by kriging interpolation, subsidence basin is obtained by DEM differential processing, and the subsidence basin is filtered by combining median filter and bilateral filter combination method, so as to obtain high-precision subsidence basin data, which provides support for the inversion of ground subsidence parameters, land reclamation and ecological restoration in the mining area (Fig. 1).

2 Materials and methods

2.1 Overview of the study area

The study area is located in the inner Mongolia Autonomous Region Ordos City Xinneng Mining Co., Ltd. Wangjiata Coal 3S201, in the influence

Fig. 1 Geographic location and schematic diagram of the mining area: **a** The observation range and flight route of the working surface UAV-LiDAR **b** the surface topography of the detection area



range of the working surface mining. The strike length of the working face is 1153 m. The tendency length is 256 m, and the average mining depth of the working surface is 210 m, respectively. The coal seam thickness range is 2.5–2.8 m, with average thickness and coal seam inclination angle of 2.65 m and 2°, respectively. The upper slate of the coal seam is sandy stone with medium-hard lithology. The basic roof is semi-hard sandy mudstone with an average thickness of 6 m, and the comprehensive histogram of the coal seam is shown in Fig. 2. The working surface is re-operated from October 7, 2020 to January 20, 2021. The location of the working face in the mining area is shown in Fig. 1, (a) is the route map and working surface range of the drone, and (b) the topographic map of the mining area.

2.2 Data acquisition and processing methods

2.2.1 UAV-LiDAR data acquisition

The data collection process includes monitoring area survey and data collection, airspace application, control point, monitoring point measurement, UAV path planning, ground reference station installation, and point cloud collection. The steps used in field data acquisition using UAV LiDAR are as follows:

- (1) Set up the base station: Before measurement, a suitable location near the measurement area is selected to set up the GPS base station, thus ensuring accurate spatial coordinates of the collected point cloud data. After data acquisition, the ground reference static station data is first selected, then the Post-Processing Kinematic technique is applied to the data collected by the IMU/GPS to ensure accurate POS (Position and Orientation System) data;
- (2) LiDAR activation: A phone is first connected to a LiDAR Wi-Fi hotspot, and then an application software combined with a scanner is employed to perform data acquisition and collection using the POS static alignment;
- (3) UAV flight control: The flight control software is used to actuate the UAV to perform the flight mission and drive the flight path, thus ensuring

UAV-data collection according to a pre-established route;

- (4) After completing the flight mission, the UAV is first returned and turned off, and then the scanner and POS are stopped after the UAV lands safely.

In this study, the DJI M600Pro UAV, equipped with the smart beak ARS-450i laser measurement system for data acquisition operations, is used to monitor subsidence in the mining area. The data acquisition process is shown in Fig. 3. The on-site acquisition diagram is shown in Fig. 4.

2.2.2 Point cloud data solution method

UAV-LiDAR point cloud data solving methods include POS solving, coordinate conversion, point cloud filtering, and ground point extraction.

(1) POS solution.

UAV-LiDAR technology requires GPS reference stations to calibrate the signals of the UAV's GPS, or multiple reference stations can be used to improve accuracy and inspection errors. POS solution mainly uses the combination of GNSS (Global Navigation Satellite System) static data and POS data (mobile station GNSS, IMU, and odometer data) collected by the base station and outputs high-precision positioning data required by the data merging software (Ma et al. 2014). In this study, the IE (Inertial Explorer) software is used to calculate, when importing base station data into engineering calculations. The geodetic coordinates of the collected database are first entered, and then the GNSS data are solved using a bidirectional algorithm in the IE to determine the flight path of the UAV. The GNSS and IMU data are then combined using the Tight Coupling technique to solve the high-precision flight position and attitude.

(2) Merging solution and coordinate converter.

Merging solution consisted of merging the raw data collected by the UAV LiDAR system with the processed high-precision POS data using HD Data Combine software to generate a point cloud file in *hls* or *las* or *xyz* format for further processing (Yang et al. 2018). The Gaussian three-dimensional projection coordinates collected by the LiDAR system (latitude, longitude, and ellipsoidal height) under the WGS84 ellipsoid are first converted to the local coordinate system to be applied. RTK dynamic measurement is used to measure some ground flat

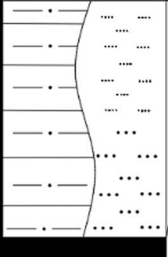





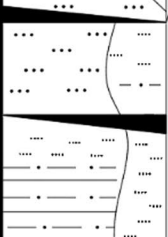
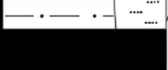
Lithology columnar 1:500	Rock name	MAX — MIN	Lithology description
		Average thickness	
	Light gray fine sandstone or Dark gray sandy mudstone	9.73—29.93	Fine sandstone: light gray, thick layered, wavy bedding, with abundant coal shavings and a small amount of plant fossil fragments in the upper part, locally containing mud inclusions, mud filled gaps, semi hard; Sandy mudstone: dark gray, thin layered, with a sandy and muddy structure, with plant fossils visible, interlaced bedding, semi hard.
		15.4(5)	
	2-2 lower coal	1.05—4.42	Coal: black, with black brown streaks, mainly dark coal, interbedded with bright coal and silk charcoal, block shaped, weak asphalt luster, and developed cracks in some areas, belonging to semi dark coal.
		3.21(5)	
	Dark gray sandy mudstone interbedded with coal	5.23—9.25	Siltstone: light gray, thick layered, wavy bedding, with abundant coal shavings and a small amount of plant fossil fragments in the upper part, locally containing mud inclusions, mud filled gaps, semi hard; Sandy mudstone: dark gray, thin layered, with a sandy and muddy structure, with plant fossils visible, interlaced bedding, semi hard.
		7.4	
	Light gray siltstone or Dark gray sandy mudstone	2.69—7.17	Siltstone: light gray, thick layered, wavy bedding, with abundant coal shavings and a small amount of plant fossil fragments in the upper part, locally containing mud inclusions, mud filled gaps, semi hard; Sandy mudstone: dark gray, thin layered, with a sandy and muddy structure, with plant fossils visible, interlaced bedding, semi hard.
		4.5	
	3-1 coal	2.5-2.8	Coal: black, with black brown stripes, mainly composed of dark coal, block like structure, asphalt luster, dull type. Charcoal containing, dull type. Sandy mudstone: dark gray, thin layered, with plant fossils visible, semi hard, located in the middle and lower part of the coal seam, with a coal seam structure of 2 (0.4) 0.65m.
		2.65	
	Dark gray sandy mudstone or gray white powdery fine sandstone, interbedded with coal seam	4.30-16.69	Dark gray sandy mudstone: thin layer with plant fossils, wavy texture, sand, mudstone structure, semi hard. Fine grained sandstone: grayish white, medium thick layered, mainly composed of quartz feldspar, with a small amount of mica debris, visible coal and dark rock debris, uniform bedding, semi hard; Sandwich 0.65m coal line, intermittently distributed.
		7.5(5)	
	Grey white powdery fine sandstone or dark gray sandy mudstone, interbedded with coal	24.67-42.17	Fine grained sandstone: grayish white, medium thick layered, with a fine-grained sand like structure, with plant fossils visible, interlaced bedding, semi hard; Medium grained sandstone: grayish white, medium thick layered, mainly composed of quartz feldspar, with a small amount of mica debris, medium grained sand like structure, semi hard; Sandy mudstone: dark gray, thin layer, sandy mudstone structure, with plant fossils visible, wavy texture, semi hard; Intercalated with 0.75m coal, intermittently distributed.
		35.5(5)	
	4-1 coal	1.73-2.04	Black, with black brown streaks, dominated by dark coal, interbedded with bright coal, block like, weak asphalt luster, belonging to semi dark coal.
		1.88(5)	

Fig. 2 The comprehensive histogram of the coal seam

and unobstructed point coordinates, RTK measurement selects the original ellipsoid to select the ellipsoid of WGS-84, and the target coordinate system selects the ellipsoid of the local coordinate system (Beijing 54 coordinate system). Using the

coordinates of these points, seven or four parameters plus elevation fitted parameters are calculated, and the POS-solved coordinates are converted into the coordinates of the local coordinate system (54 coordinates). The coordinate points of the absolute

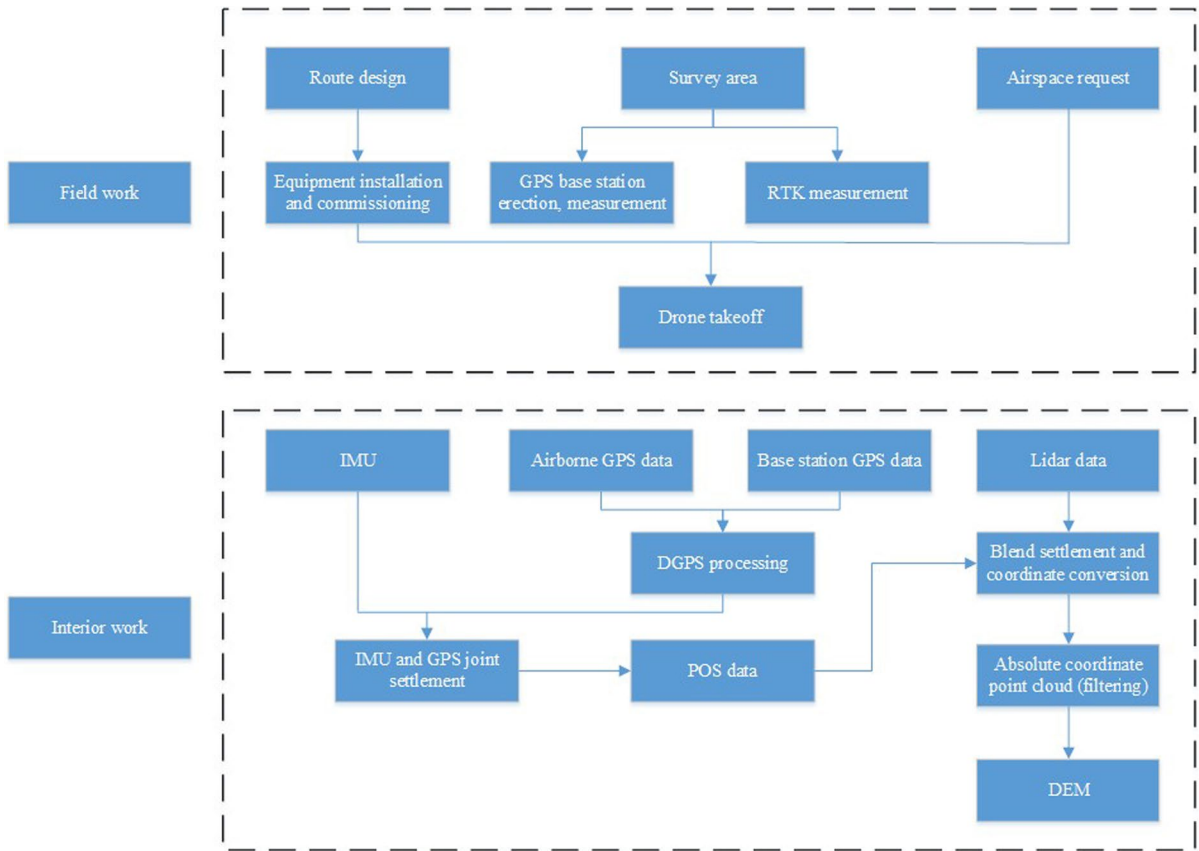


Fig. 3 Technical flow chart

Fig. 4 Field data acquisition operations



coordinate conversion parameter are obtained from the WGS84 coordinates and the Beijing 54 coordinates measured by CORS-RTK.

(3) Point cloud filtering and ground point extraction.

The point cloud data acquired by the UAV LiDAR data includes ground points, buildings, vegetation, transmission towers, and other features (Jiao et al. 2018). Therefore, to ensure high-precision terrain data for ground subsidence observation, the point cloud data are filtered using Cloth Simulation Filter (CSF) to separate ground from non-ground points. After multiple runs, the cloth resolution, maximum number of iterations, and the classification threshold of the CSF algorithm are fixed at 1, 850, and 0.55, respectively. Ground point data with high-resolution are used for the generation of DEM.

2.2.3 Measurement accuracy analysis of UAV-LiDAR

(1) Instrument error

Zhi beak ARS-450i laser measurement system as an example, inertial navigation plane positioning accuracy of 1cm, elevation positioning accuracy of 2cm, the scanner’s ranging accuracy of 5mm/100m, ranging accuracy by the flight altitude of the flight is more influential, the general UAV flight relative height is not easy to be too high, so take the flight altitude of 100m as an example, at this time by the scanning instrument ranging accuracy of 5mm at this time. According to the nominal accuracy, the overall system performance of inertial navigation and the scanner’s plane accuracy m_{yh} and elevation accuracy m_{yv} are 5cm each.

(2) Control of measurement errors

The LiDAR is equipped with M600 UAV, and the GNSS module is added based on M600 UAV, its horizontal positioning accuracy is 1cm + 1ppm, vertical positioning accuracy is 2cm + 1ppm, and taking a flight distance of 2 km as an example, the horizontal accuracy $m_{kh1}=3cm$, vertical accuracy $m_{kv1}=4cm$; As the ground needs to make static RTK, for COSHIDA iRTK5, it’s plane positioning accuracy $m_{kh2}=2.5mm$, and elevation positioning accuracy $m_{kv2}=5mm$.

$$\begin{cases} m_{kh} = \sqrt{m_{kh1}^2 + m_{kh2}^2} = 3.01cm \\ m_{kv} = \sqrt{m_{kv1}^2 + m_{kv2}^2} = 4.03cm \end{cases} \quad (1)$$

(3) Platform error

The error of the UAV flight platform is taken as 5cm.

Based on the above calculation, according to the law of error propagation, the theoretical error formula of the measured point cloud data is:

$$\begin{cases} m_h = \sqrt{m_{kh}^2 + m_{yh}^2 + m_{ph}^2} = 5.8cm \\ m_v = \sqrt{m_{kv}^2 + m_{yv}^2 + m_{pv}^2} = 6.4cm \end{cases} \quad (2)$$

3 Subsidence basin extraction and filtering methods

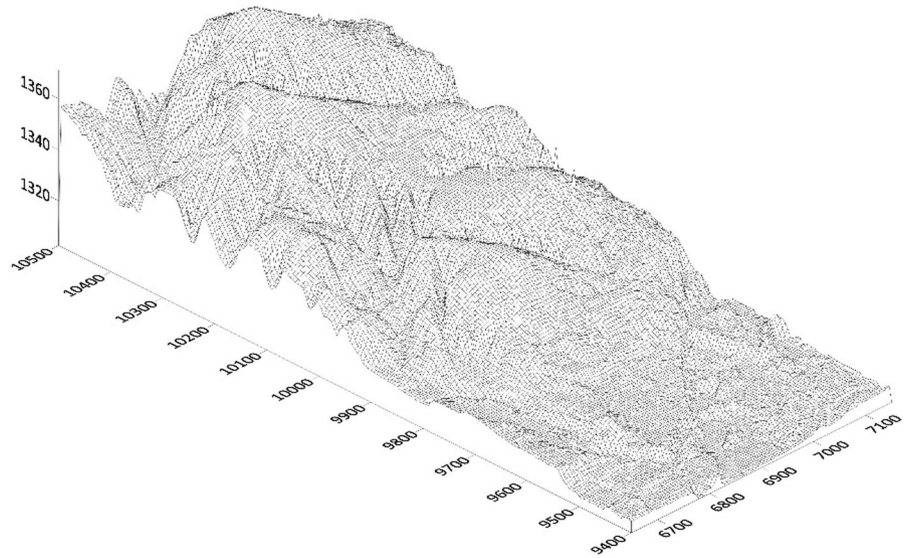
The UAV-LiDAR monitoring principle is to scan the same area twice at different times to obtain a digital ground model DEM of the surface at two times, and the difference between the two phases of DEM can obtain the measured sinking value of the surface of the monitoring area. Therefore, it is crucial to establish a high-precision DEM.

3.1 DEM establishment method

The digital elevation model refers to the digital morphological attribute information on terrain surface elevation. The regular grid is one of the most common data structures for DEM. The regular grid DEM represents the terrain in a matrix grid formed by the elevation of a series of terrain points arranged in equal intervals in the X and Y directions. In this experiment, GIS kriging interpolation method is used to obtain the estimation results of optimal unbiased elevation, as shown in Fig. 5.

After modeling the DEM, the elevation accuracy of the model is assessed by exporting the three-dimensional coordinates (x, y, and z) of the surface DEM and determining the difference in the elevation z is in each x and y coordinate to calculate the variance.

Fig. 5 DEM generated by the kriging interpolation method



$$Z_p^* = \sum_{i=1}^n z_i w_i \quad (3)$$

where W_i is the weight vector; the z_i is the elevation of the ground point, and the Z_p^* is the elevation of the interpolation value.

In this paper, Kriging interpolation method is used, which is an estimation method using variational function to determine the optimal weight W_i . Weights measure a numerical uncertainty through variance and describe the confidence of a statistical parameter. Each known data value in the Kriging interpolation method and each missing data value has a related variance value. Expressed on a normalized scale (normalized to 0–1), the variance function is completely reliable if it is a constant with a variance of 0, while a value is completely unreliable if it is completely unreliable. The variance in the kriging method is a quadratic function of the weight. For example, data with high reliability and a variance of 0, requires an assignment of all missing data a value equal to this value since there is only one known point. Therefore, the missing value estimation near and away from the known point can result in high and low reliability, respectively. In other words, the uncertainty increases with increasing the distance from the known points.

The variance of each known value can be calculated using empirical variance function models,

namely linear, spherical, logarithmic, and Gaussian, thus allowing the estimation of the variance value between known and surrounding estimated values. These functions have a minimum value (usually 0) at the location of a known data point and a maximum value (usually 1) after a certain distance from that point (i.e., a range), and all locations outside the range are considered unaffected by the known point data.

$$\sigma_z^2 = w_1 \gamma d_{1p} + w_2 \gamma d_{2p} + w_3 \gamma d_{3p} + \lambda \quad (4)$$

where w_1, w_2, w_3 represent the weight vectors in the x, y, z direction, d_{1p}, d_{2p}, d_{3p} interpolated points to known points in the x, y, z direction, respectively; γ represents the function model, in this case the linear model; λ is the weight coefficient.

3.2 Subsidence basin filtering methods

The subsidence basin is obtained from the measured elevation data, which is easily affected by the measurement error and will cause obvious noise. The subsidence is subtracted by quantifying the temporal change of DEM, showing significant noise. Indeed, there are two filtering methods. The first one consists of filtering separately the surface DEM phases, followed by subtracting to obtain smooth subsidence classes. The second consists of filtering the noise of the original subsidence classes using a filtering

algorithm. In this study, the adaptive median filtering method allowing direct noise filtering is used on the subsidence classes to eliminate the sudden change in terrain elevation. In addition to this method, a bilateral filter is used to maintain the edge of the study area while filtering out noise.

(1) Median filter

The median filter is a sort-based nonlinear filter that eliminates digital signal interference and maintains signal edges. This technique has been widely used in two-dimensional digital filtering. This technique consists of selecting an odd template window to move along the rows or columns of the two-dimensional digital matrix and replacing the values in the window with the median value, according to the following equation:

$$g(x, y) = \text{median}\{f(x - i, y - j)\}, \quad (i, j) \in S \quad (5)$$

where $f(x,y)$, $g(x,y)$ are the pre-process matrix and post-process matrix, respectively, and S is the template window.

The larger the template of median filtering, the more noise is filtered out. However, the deviation of the center value of the template window from the observed value can result in erroneous results. Therefore, a 3*3 template is used in the filtering. A schematic of median filtering is shown in Fig. 6

(2) Bilateral filter

A bilateral filter is a filter that preserves the edge when removing noise, such as Gaussian distribution. This effect can be achieved based on two main functions. The first function determines the filter coefficient based on the geometric space distance, while the second consists of determining the difference between the neighboring grid

numbers. In the bilateral filtering algorithm, the output grid value is a weighted combination of the adjacent mesh values, which can be expressed by the following equation:

$$g(i, j) = \frac{\sum_{k,l} f(k, l)w(i, j, k, l)}{\sum_{k,l} w(i, j, k, l)} \quad (6)$$

The weight coefficient $w(i, j, k, l)$ depends on the kernel domain.

$$d(i, j, k, l) = \exp\left(-\frac{(i - k)^2 + (j - l)^2}{2\sigma_d^2}\right) \quad (7)$$

and the value range kernel

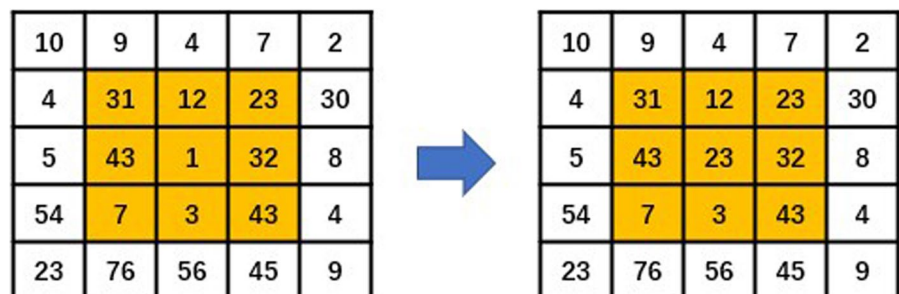
$$r(i, j, k, l) = \exp\left(-\frac{\|f(i, j) - f(k, l)\|^2}{2\sigma_r^2}\right) \quad (8)$$

$$w(i, j, k, l) = \exp\left(-\frac{(i - k)^2 + (j - l)^2}{2\sigma_d^2} - \frac{\|f(i, j) - f(k, l)\|^2}{2\sigma_r^2}\right) \quad (9)$$

where (i, j) represents the grid position, (k, l) represents the range centered on (i, j) $(2N + 1) (2N + 1)$, $f(k, l)$ represents the grid value involved in the calculation, σ_d^2 participates in calculating the variance of the grid position distance, and σ_r^2 participates in calculating the variance of the grid value.

Considering the difference between the value domain and the air domain, compared with the difference between the traditional Gaussian filter or the mean filter of a single spatial domain and/or value domain, it can better remove noise while retaining characteristics.

Fig. 6 Schematic diagram of the median filter principle



4 Results and discussion

4.1 The results of the subsidence basin are obtained

In this study, the maximum and minimum values of X and Y are first set for each data, and then vegetation-free point cloud data are gridded using a grid spacing of 5 m. In total, 22,321 points of the three-dimensional coordinates are obtained according to the results of the kriging interpolation method. The first and second DEM data are established On August 24, 2020 and March 16, 2021, respectively, by collecting data using UAV LiDAR (Fig. 7a and b). In this study, the accuracy of the kriging interpolation method is assessed using by calculating the elevation variance of the established DEM according to Eq. (3). The center points of each grid of the two observational data are considered in the calculation. The overall variance of the entire mesh is then determined using the following equations:

$$\sigma_1^2 = \frac{\sum_{i=1}^n \sigma_{1i}^2}{22321} = 0.000236\text{m}^2 \sigma_1 = 0.015\text{m}$$

$$\sigma_2^2 = \frac{\sum_{i=1}^n \sigma_{2i}^2}{22321} = 0.000173\text{m}^2 \sigma_2 = 0.013\text{m}$$

It can be seen from the calculation results that the values of the overall variance of the two points are slightly similar and are in the same order of magnitude ($\sigma_1=15$ mm; $\sigma_2 = 13$ mm), suggesting a reliable and stable processing method of DEM.

Surface subsidence basins can be obtained by two phases of DEM differential processing, that is, the second observation of DEM2 minus the first observation of DEM1 to obtain, from small to large traversal of all grid z values, the maximum subsidence value can be obtained. The subsidence basin obtained is shown in Fig. 8a and b, and according to GPS measurements, the true maximum sinking value of this area is -2.84m . From Fig. 8b, there is obviously

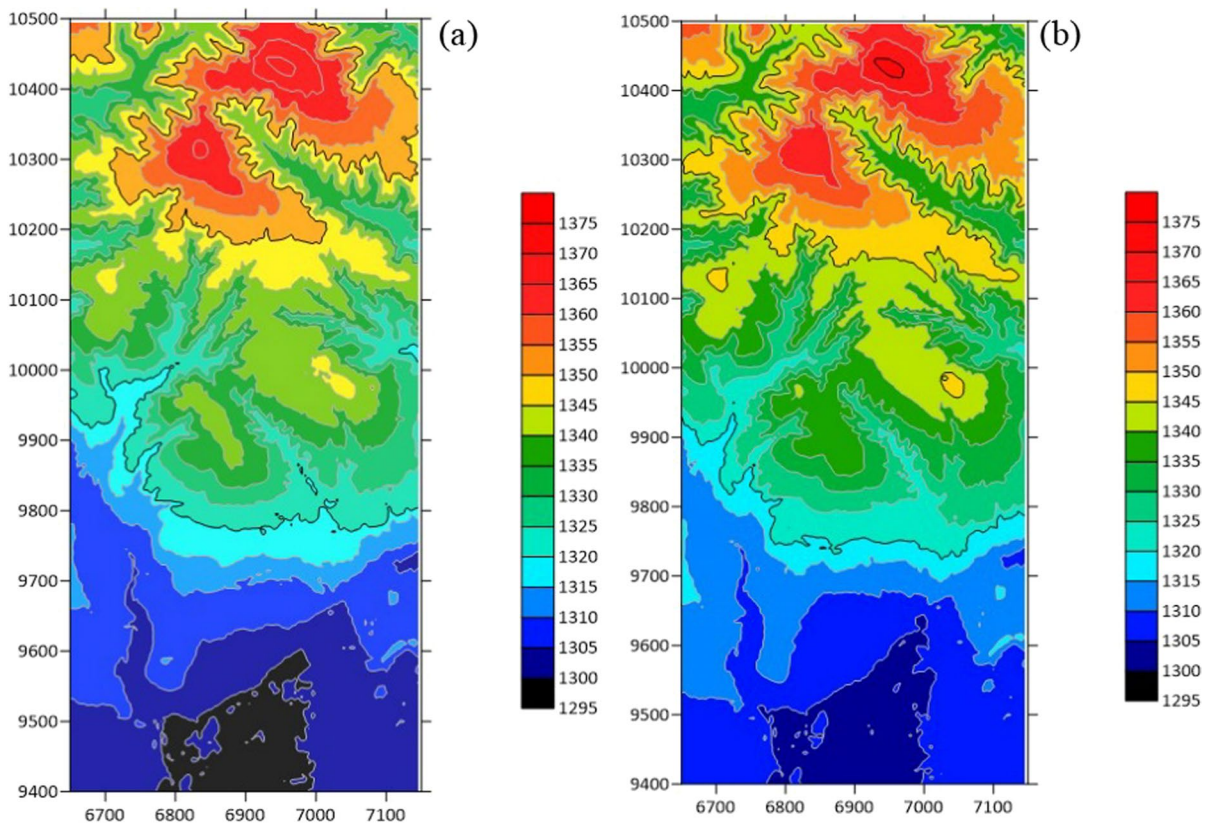


Fig. 7 Surface DEM established by point cloud interpolation, **a** August 24, 2020; **b** March 16, 2021

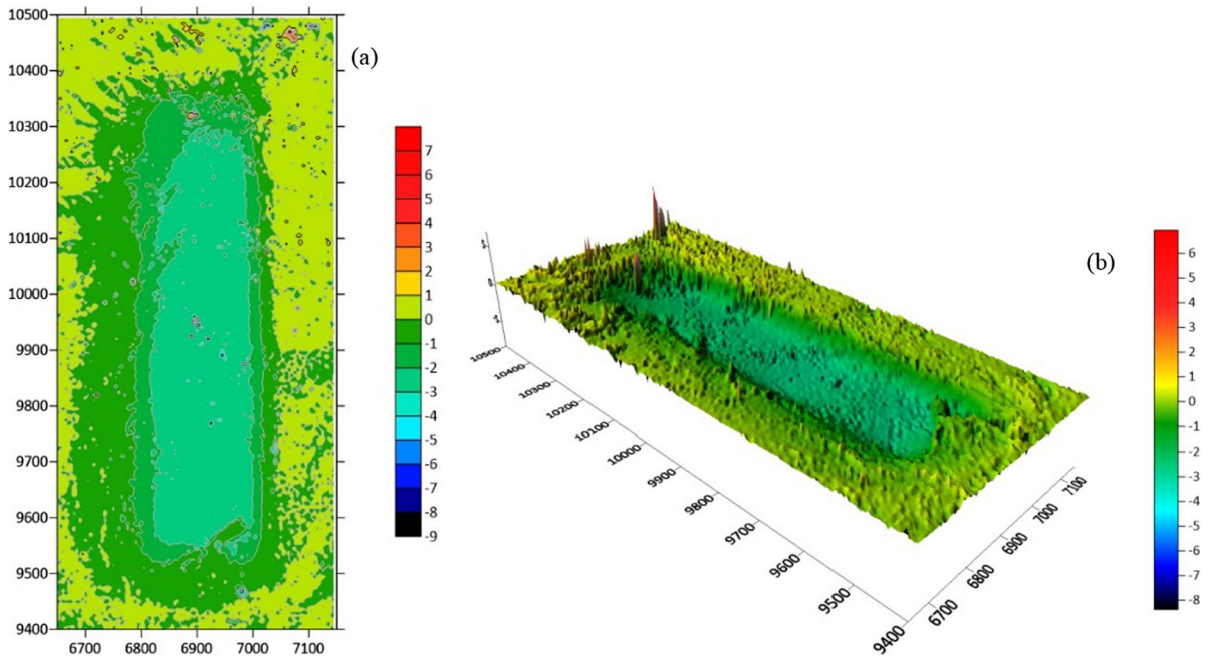


Fig. 8 Ground subsidence obtained by two phases of DEM differential treatment. **a** DEM of the ground subsidence **b** 3D view of the ground subsidence

some noise in the subsidence basin, resulting in a sudden change in the sinking value of the basin, so the subsidence basin needs to be filtered.

4.2 Subsidence basin noise filtering results

The results showed that the noise of the original DEM1 affected the contour line generation (Fig. 9a), while the median filtering technique removed most

random noise in DEM2 while maintaining the main features (Fig. 9b). The edge of the mining area subsidence is further processed using bilateral filtering (Hu and Li 2012). By comparing the contour lines of the boundary of the three graphs processed by the median filter, significant variation in the DEM2 and DEM1 edges is found, suggesting a poor effect of the median filtering technique on the study area edge, which is not conducive to the extraction of

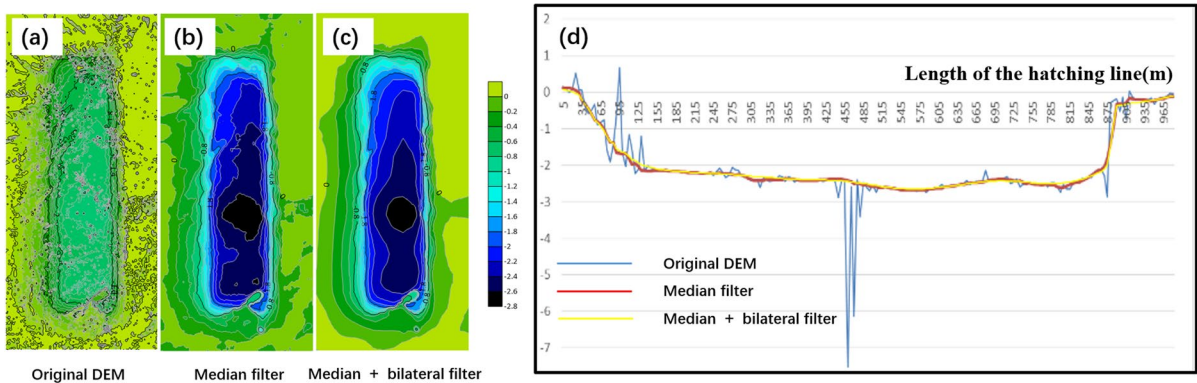


Fig. 9 Results of filtering processing on subsidence in the study area, **a** original DEM1, **b** Median filter DEM2, **c** Median + bilateral filter DEM3, **d** subsidence basin profile

the subsidence boundary. The median filtering technique is followed by bilateral filtering processing to generate the DEM3 (Fig. 9c). The results revealed a smooth contour line in the subsidence boundary with similar shapes.

The profile lines are drawn at the same position as the DEM center lines of the three subsiding basins, as shown in Fig. 9d. It can be seen that the original DEM profile line is obviously messy and contains a large number of abrupt elevation points. This indicates that the true subsidence is difficult to obtain based on the original DEM. Whereas, the DEM profile lines of the median filter revealed a lack of noise with smoother contour lines. However, at the edge of the subsidence area in the crosshatch, the subsidence value obtained following median filter processing is smaller than that obtained using combined median and bilateral filters. In addition, compared with the results of the median filtering processing, the combined filtering method revealed linearly smoother lines with values close to the observed value at the edge of the basin (Fig. 10). Therefore, the combined median and bilateral filtering

methods can better retain the critical value area of the boundary deformation during the noise removal process, thus resulting in better extraction of the subsidence boundary.

The GPS-RTK is used to measure the elevation at multiple detection points, to assess the accuracy of the subsidence values and delimitation area using the following formula:

$$\Sigma = \sqrt{\frac{[vv]}{n-1}} \quad (10)$$

where v is the error value and n are the number of stations.

The calculation results are summarized in Table 1. The error of the subsidence distribution ranged from 0.016 to 0.59 m, with a median value of 0.039 m.

4.3 Discussion and suggestions

The problem of rock formation and surface deformation caused by coal mining is particularly

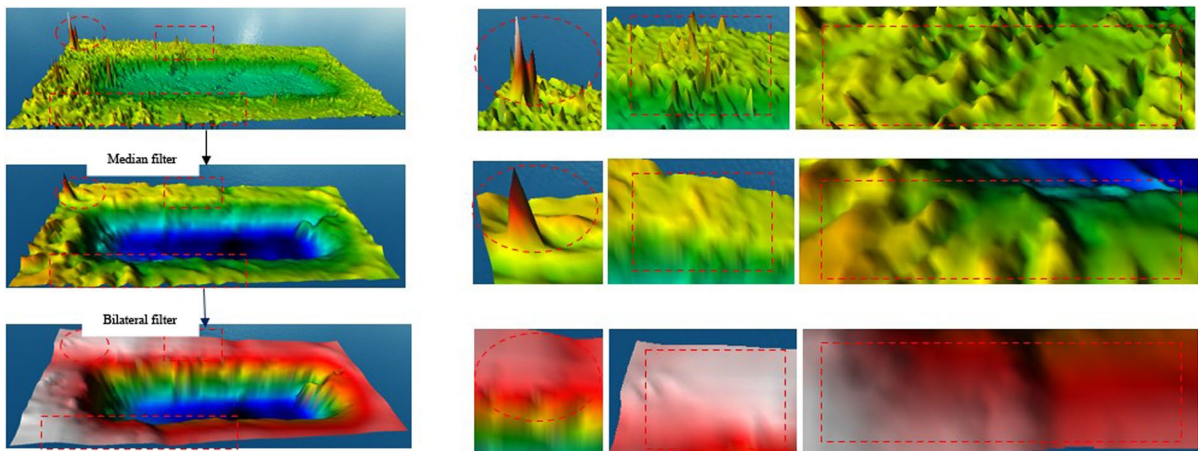


Fig. 10 Comparison of local details in the filtered subsidence area

Table 1 Comparison between measured subsidence and model values

Measure points	Observatory data (m)	Model data (m)	error (m)	Measure points	Observatory data (m)	Model data (m)	error (m)
1	-0.155	-0.129	0.026	4	-1.747	-1.731	0.016
2	-2.564	-2.623	-0.059	5	-0.955	-0.915	0.040
3	-2.270	-2.253	0.017				

The standard deviation $\sigma = 0.039$ m

prominent in western China, where the ecological environment is extremely fragile, seriously restricting the sustainable development of coal mining enterprises and threatening people's lives. Shallow burial depths, large mining heights, rapid and comprehensive mechanization, and high-intensity mining have become common practices in the western region. However, the rock formations and surface movements caused by mining have resulted in wide-ranging and significant damage. Conventional surface mobile observatories are unable to provide comprehensive monitoring of mining damage. These methods are costly, labor-intensive, and inaccurate in ground subsidence monitoring. UAV measurements provide new technical ways to address these challenges. UAV photogrammetry uses unmanned aerial vehicles as a platform to obtain rapidly comprehensive surface data. Indeed, this technology has the advantages of flexible mobility, high efficiency and precision, and low operating cost. In this study, UAV-LiDAR is used to determine the subsidence data of the mining area in Inner Mongolia, providing a valuable database for ecological environment monitoring in the mining area and subsequent ecological restoration and land reclamation.

At present, the relevant processes and data quality standards of ground subsidence in mining areas monitored by UAV-LiDAR technology do not have the same standard as those of traditional observatories. Therefore, this study focused on the application methods and accuracy assessments of UAV-LiDAR in mining areas. UAV-LiDAR monitoring technology showed high subsidence monitoring accuracy. The point cloud data collected by UAV LiDAR is large and informative, allowing the observation of large-scale ground subsidence.

However, due to measurement error, the resulting subsidence area may exhibit noise that can be removed using appropriate filtering methods. Laser point cloud data interpolation used in DEM generation can result in an accuracy loss since the size of the interpolated mesh affects the interpolation accuracy. The smaller the mesh, the higher the accuracy, and the larger the amount of data. Indeed, the size of the actual grid can be determined based on the accuracy of the data and the comprehensiveness of the monitoring.

5 Conclusions

The extensive mechanization of mining activity in the western China has resulted in rapid extraction and a short mining cycle. In this study, the UAV-LiDAR technology is used to monitor the ground subsidence of the mining area. The corresponding technical processes and data processing methods are evaluated. The results demonstrated that the use of UAV-LiDAR can effectively and rapidly monitor the ground subsidence of the mining area at a large scale, and accurately determine the morphology of the entire western mining area and the cross-section line of the subsidence area basin. Indeed, high-intensity ground subsidence deformation of the western mining area is determined accurately by UAV-LiDAR. Moreover, the large number of point cloud data obtained can provide data support for related research.

The accuracy of the DEM generated by the UAV-LiDAR data is 15 mm, while the mean square error of the subsidence area, obtained by the two-phase differencing (August 24, 2020 and March 16, 2021) DEM, is 39 mm, demonstrating that the accuracy of the entire subsidence DEM model can meet the engineering needs of mining subsidence monitoring in the mining area.

The median and bilateral filters are used in the DEM of the subsidence area to address the noise points generated from point cloud data. The results demonstrated that these filters can maintain the high-precision surface and mathematical characteristics of the DEM, thus allowing effective mining surface damage monitoring and providing support for the monitoring of the ecological environment of the mining area and the subsequent ecological restoration and land reclamation.

Acknowledgements The research has been financially supported by the Natural Science Foundation Project (Grant Numbers 53904174). The authors would like to thank the editor and reviewers for their contributions on the paper.

Author contributions Conceptualization, YX; methodology, SA and LY; software, XW; formal analysis, DZ and YX; project administration, SA and YX; funding acquisition DZ. All authors have read and agreed to the published version of the manuscript.

Funding Supported by the Academician Workstation in Anhui Province, Anhui University of Science and Technology; Huainan Natural Science Foundation Project (Grant Numbers 53904174).

Data Availability The data that support the findings of this study are available from the corresponding author, [Shikai An], upon reasonable request.

Declarations

Ethics approval and consent to participate Not applicable, Ethics approval was not required for this research.

Consent to publish All authors consent to the publication of this paper.

Competing interests The authors declare that they have no known competing financial interests or personal relationships that could have appeared to influence the work reported in this paper.

Open Access This article is licensed under a Creative Commons Attribution 4.0 International License, which permits use, sharing, adaptation, distribution and reproduction in any medium or format, as long as you give appropriate credit to the original author(s) and the source, provide a link to the Creative Commons licence, and indicate if changes were made. The images or other third party material in this article are included in the article's Creative Commons licence, unless indicated otherwise in a credit line to the material. If material is not included in the article's Creative Commons licence and your intended use is not permitted by statutory regulation or exceeds the permitted use, you will need to obtain permission directly from the copyright holder. To view a copy of this licence, visit <http://creativecommons.org/licenses/by/4.0/>.

References

- Aumann G, Ebner H, Tang L (1991) Automatic derivation of skeleton lines from digitized contours. *ISPRS J Photogr Remote Sens* 46(5):259–268
- Bai W (2017) Mining subsidence monitoring method based on laser scanning technique. *Metal Mine* 487(01):132–135
- Bai J, Li S, Jiang Y et al (2019) An extension theoretical model for grouting effect evaluation in sand stratum of metro construction. *KSCE J Civ Eng* 23(5):2349–2358
- Bai J, Zhu Z, Liu R et al (2021) Groundwater runoff pattern and keyhole grouting method in deep mines. *Bull Eng Geol Env* 80:5743–5755
- Dawei Z, Lizhuang Q, Demin Z et al (2020) Unmanned Aerial Vehicle (UAV) photogrammetry technology for dynamic mining subsidence monitoring and parameter inversion: a case study in China. *IEEE Access* 8:16372–16386
- Fan L, Ma X, Li Y et al (2017) Geological disasters and control technology in high intensity mining area of western China. *J China Coal Soc* 42(2):276–285
- Ge D, Dai K, Guo Z et al (2019) Early identification of serious geological hazards with integrated remote sensing technologies: thoughts and recommendations. *Geomat Inf Sci Wuhan Univ* 44(07):949–956
- He G, Yang L, Ling G et al (1991) Mining subsidence science[M]. China University of Mining and Technology Press, Xuzhou
- Hu J, Li S (2012) The multiscale directional bilateral filter and its application to multisensor image fusion. *Inform Fusion* 13(3):196–206
- Hutchinson MEANUDEM Version 4.6. Centre for Resources and Environmental Studies, Australian National University Canberra. 1997
- Jiao X, Hu H, Lian X (2018) Deformation monitoring method of the buildings in mining area based on 3D laser scanning technique. *Metal Mine* 502(04):150–153
- Kršák B, Blišťan P, Paulíková A, Puškárová P, Kovanič L, Palková J, Zelížňáková V (2016) Use of low-cost UAV photogrammetry to analyze the accuracy of a digital elevation model in a case study. *Measurement* 91:276–287
- Lanari R, Fomaro G, Riccio D et al (1997) Generation of digital elevation models by using SIR-C/X-SAR multi-frequency two-pass interferometry: the Etna case study. *IEEE Trans Geosci Remote Sens* 34:1097–1140
- Li J, Yang C, Hu Y et al (2020) Application research of UAV-Lidar in detection of underground goaf. *Metal Mine* 12:168–172
- Ling G, Wu K et al (1994) A research on analysis method of mining subsidence parameters for space problem and its application. *J China Univ Min Technol* 23(2):64–69
- Ma D, Cui J, Wang S (2014) Application and research of 3D laser scanning technology in steel structure installation and deformation monitoring. *Appl Mech Mater* 580:2838–2841
- Ma Q, Liu XL, Tan YL et al (2023) Numerical study of mechanical properties and microcrack evolution of double-layer composite rock specimens with fissures under uniaxial compression. *Eng Fract Mech* 289(2):109403. <https://doi.org/10.1016/j.engfracmech.2023.109403>
- Research Group of National Key Basic Research Program of China (2013CB227900) (2017) (Basic Study on Geological Hazard Prevention and Environmental Protection in High Intensity Mining of Western Coal Area). Theory and method research of geological disaster prevention on high-intensity coal exploitation in the west areas. *Journal of China Coal Society* 42(2):267–275.
- Wu Q, Liu H, Zhang H et al (2019) Discussion on the nine aspects of addressing environmental problems of mining. *J China Coal Soc* 44(1):10–22
- Yang Z, Li Z, Zhu J, Feng G, Wang Q, Hu J, Wang C (2018) Deriving time-series three-dimensional displacements of mining areas from a single-geometry InSAR dataset. *J Geodesy* 92:529–544
- Yang Q, Tang F, Wang F et al (2023) A new technical pathway for extracting high accuracy surface deformation

information in coal mining areas using UAV LiDAR data: an example from the Yushen mining area in western China. *Measurement* 218:113220

Zhang W, Qi J, Wan P, Wang H, Xie D, Wang X, Yan G (2016) An easy-to-use airborne LiDAR data filtering method based on cloth simulation. *Remote Sensing* 8(6):501

Zhou QY, Neumann U (2013) Complete residential urban area reconstruction from dense aerial LiDAR point clouds. *Graph Models* 75:118–125

Zhou D, Wu K, Chen R et al (2014) GPS/terrestrial 3D laser scanner combined monitoring technology for coal mining

subsidence: a case study of a coal mining area in Hebei, China. *Nat Hazards* 70(2):1197–1208

Publisher's Note Springer Nature remains neutral with regard to jurisdictional claims in published maps and institutional affiliations.